Light absorption from particulate impurities in snow and ice determined by spectrophotometric analysis of filters

Thomas C. Grenfell,[1,*] Sarah J. Doherty,[2] Antony D. Clarke,[3] and Stephen G. Warren[1]

[1]Department of Atmospheric Sciences, Box 351640, University of Washington, Seattle, Washington 98195, USA

[2]Joint Institute for the Study of Atmosphere and Ocean, Box 355762, University of Washington, Seattle, Washington 98195, USA

[3]School of Ocean and Earth Sciences and Technology, University of Hawaii, Honolulu, Hawaii 96822, USA

*Corresponding author: tcg@atmos.washington.edu

Received 3 June 2010; revised 26 January 2011; accepted 27 January 2011; posted 28 January 2011 (Doc. ID 129493); published 5 May 2011

Light absorption by particulate impurities in snow and ice can affect the surface albedo and is important for the climate. The absorption properties of these particles can be determined by collecting and melting snow samples and extracting the particulate material by filtration of the meltwater. This paper describes the optical design and testing of a new instrument to measure the absorption spectrum from 400 to 750 nm wavelength of the particles collected on filters using an "integrating-sandwich" configuration. The measured absorption is shown to be unaffected by scattering of light from the deposited particulates. A set of calibration standards is used to derive an upper limit for the concentration of black carbon (BC) in the snow. The wavelength dependence of the absorption spectra from 450 to 600 nm is used to calculate an absorption Ångstrom exponent for the aerosol. This exponent is used to estimate the actual BC concentration in the snow samples as well as the relative contributions of BC and non-BC constituents to the absorption of solar radiation integrated over the wavelength band 300 to 750 nm.

OCIS codes: 120.0120, 120.3150, 120.4640, 120.6200, 300.0300, 300.6550.

1. Introduction

At visible and near-ultraviolet wavelengths, ice is so weakly absorbing that small amounts of light-absorbing impurities can dominate the absorption of sunlight by snow. Submicrometer-sized soot particles, containing a large fraction of black carbon (BC), are produced by incomplete combustion in diesel engines, coal burning, forest fires, agricultural fires, and residential wood burning [1,2]. These particles may be carried thousands of kilometers in the atmosphere before being scavenged by raindrops or snow crystals or through dry deposition. Soil dust can also be transported large distances and can also reduce the albedo of snow and ice. Typical snow in the northern hemisphere measured in 1983–1984 was found to contain enough soot and dust to reduce its albedo by 1%–2% [3]. This small reduction is enough to be important for climate [4–6], but it is not enough to be visible to the eye or reliably detectable from satellite imagery.

Determination of the absorptivity and concentration of light-absorbing aerosols in snow or ice is therefore most reliably determined by direct sampling of the medium. The principal techniques currently available to analyze BC in snow and ice involve melting and filtration of the samples to deposit the aerosol particles onto suitable filters followed by (a) direct optical analysis of the filters [3] or (b) stepwise combustion of the deposited material, the "thermo-optical" method [7]. A third method is

0003-6935/11/142037-12$15.00/0

the single-particle soot photometer (SP2) [8,9]. The thermo-optical method has been used in several studies on snow (e.g., [10,11]). The SP2 method has been used on ice cores [12]. Here we describe the characteristics and application of a new instrument of type (a) to carry out optical determination of direct absorption of light, making use of recent advances in optical instruments including high-resolution compact spectrophotometers and stable illumination sources. We also describe a method for deriving the maximum BC concentration in the snow samples. An extension of this technique incorporating an estimate of the spectral absorption characteristics of non-BC material makes it possible to estimate the actual BC concentration and to separate the contributions of BC and other constituents to the absorption of solar radiation integrated from 300 to 750 nm.

2. Background

When the objective is to determine the effect of soot on the snow-surface energy budget rather than to quantify the carbon mass budget, the optical transmission method has the advantage that it provides a measure of absorption, which is related to the absorption of sunlight in the snowpack. Since one measures absorption directly instead of measuring particle mass and then converting it to absorption, this method avoids the need to know the mass-absorption cross section of the BC. There are additional advantages to the filter method. The filtering can easily be done in remote field camps, so it is not necessary to transport large quantities of snow from the field site. Initial estimates of effective BC loading in the snow can be made in the field via visual comparison against a set of standard filters to provide insurance against sample loss and to permit reassessment of the sampling strategy while still in the field. The sample filters are then returned to the laboratory for analysis by spectrophotometric techniques.

In prior work begun in 1985 by Clarke and Noone [3], an integrating-plate (IP) photometer [13] was used to investigate the BC content of snow in the Arctic and in the mountains of the Pacific Northwest [3,14–16]. In those studies, snow samples of 100–1000 grams were collected, melted rapidly, and passed through 0.4 μm Nuclepore filters to collect the particulate material. The filters were air dried, and transmittance was measured at four wavelengths to determine the concentration of absorbing aerosol and to provide a spectral signature for the purpose of separating BC and non-BC components. The calibration was provided by measuring the transmittance of filters with known (weighed) amounts of BC in the form of Monarch-71 soot, which had been prefiltered to produce a size distribution representative of atmospheric BC. A detailed description of the process and the characteristics of the standard soot is presented in the 1985 study [3].

Analysis of the IP photometer method [17] showed that corrections were required due to modification of the system reflectance resulting from the interaction between the particles and the collection filter. This effect can depend on the size distribution and composition of the particles, and it is particularly pronounced if large aerosol particles with weak absorption are present on the filters. These particles can produce lensing effects, modifying the absorption efficiency of the smaller absorptive aerosols behind them on the filter. If the radiation field interacting with the particles is not isotropic, they can also act to scatter light out of the field of view of the detectors, producing a spuriously enhanced attenuation that could be attributed incorrectly to absorption.

This effect is also important to recognize when conducting visual inspection of the sample filters under nonisotropic illumination, since the appearance of the filter and the comparison against the calibration filters can vary depending on the ambient illumination. Figure 1 shows photographs with a high-magnification optical microscope of the edge of the exposed area of a filter under reflected versus transmitted illumination that is essentially collimated. The apparent absorption, indicated by the contrast of the exposed area on the left and the unexposed area on the right, is seen to be sensitive to the illumination conditions. A consequence of this is that the visual estimates made in the field relative to a set of standards are uncertain and require careful control of the illumination of all filters under comparison. In addition to BC, the field filters often contain other more weakly absorbing particles with higher ratios of scattering to absorption than the soot on the standard filters. The visual estimates thus give an effective BC value as though all the material on the filter is soot. Our experience has shown that the visual comparison is best carried out under diffuse reflected illumination with the filters sitting on a white diffusing background. Additional uncertainties include personal bias and the difficulty of attempting to ignore color when comparing a brown dust-laden filter to a gray calibration filter. As will be shown below, the resulting uncertainty involved is approximately a factor of 2.

To minimize the influence of the scattering effects, an "integrating-sandwich" (ISW) technique

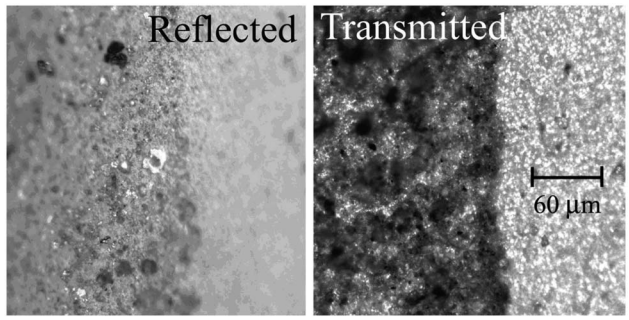

Fig. 1. Optical microscope photographs of the edge of the exposed zone on a Nuclepore filter showing significant visible differences between illumination with reflected and transmitted light. This motivates the integrating-sandwich technique, which removes the influence of scattering losses by material on the filter.

was developed and tested [18,19] that involves the introduction of a second highly scattering diffuser to surround the loaded sample filter with a radiation field that is essentially isotropic. Any light scattered by the particles is included in the multiply scattered radiation field surrounding the filter and experiences very little loss, and the light passing through the sandwich to the detector is modulated only by absorption from the material on the filter. The ISW configuration also produces an amplification of the absorption of the light due to multiple passes of the radiation through the material on the filters. The challenges with this technique are (a) that the radiation transmitted to the detector is faint, requiring either long integration times or a bright and very stable light source, and (b) that the response of the system to BC loading is nonexponential, requiring a set of standards covering the full range of filter loadings and careful calibration.

These considerations, as well as significant advances in the development of improved compact optical components, have motivated the construction of a new spectrophotometer system making use of the integrating-sandwich technique. The instrument is referred to here as an ISSW spectrophotometer, as it incorporates an integrating sandwich together with an integrating sphere.

3. ISSW System Characteristics

A schematic diagram of the system optics is shown in Fig. 2. A filter is mounted by raising the compression weight and positioning it with forceps on the bottom window. The weight is the only moving part of the system, thus avoiding difficulties with optical misalignment of the system components. It also ensures constant uniform pressure on all filter samples. White light illumination from a Dolan Jenner DC-950H light source using a 150-W quartz-halogen lamp is transmitted into a 50-mm-diameter Spectralon integrating sphere via a 6.3-mm-diameter optical fiber to produce a diffuse radiation field at the output port of the sphere. The diffuse radiation then passes through the sample cell consisting of the sample filter and an upper diffuser consisting of a quartz fiber filter mounted as shown between 50-mm-diameter sapphire windows. The upper diffuser has a reflectivity of about 0.95 and produces diffuse radiation directed from above back at the sample filter, so that the filter is diffusely illuminated from both sides. Since the reflectivity of the integrating sphere is also very high (0.99), the radiation undergoes multiple reflections through the sample filter between the upper diffuser and the integrating sphere, enhancing the absorption signal [18].

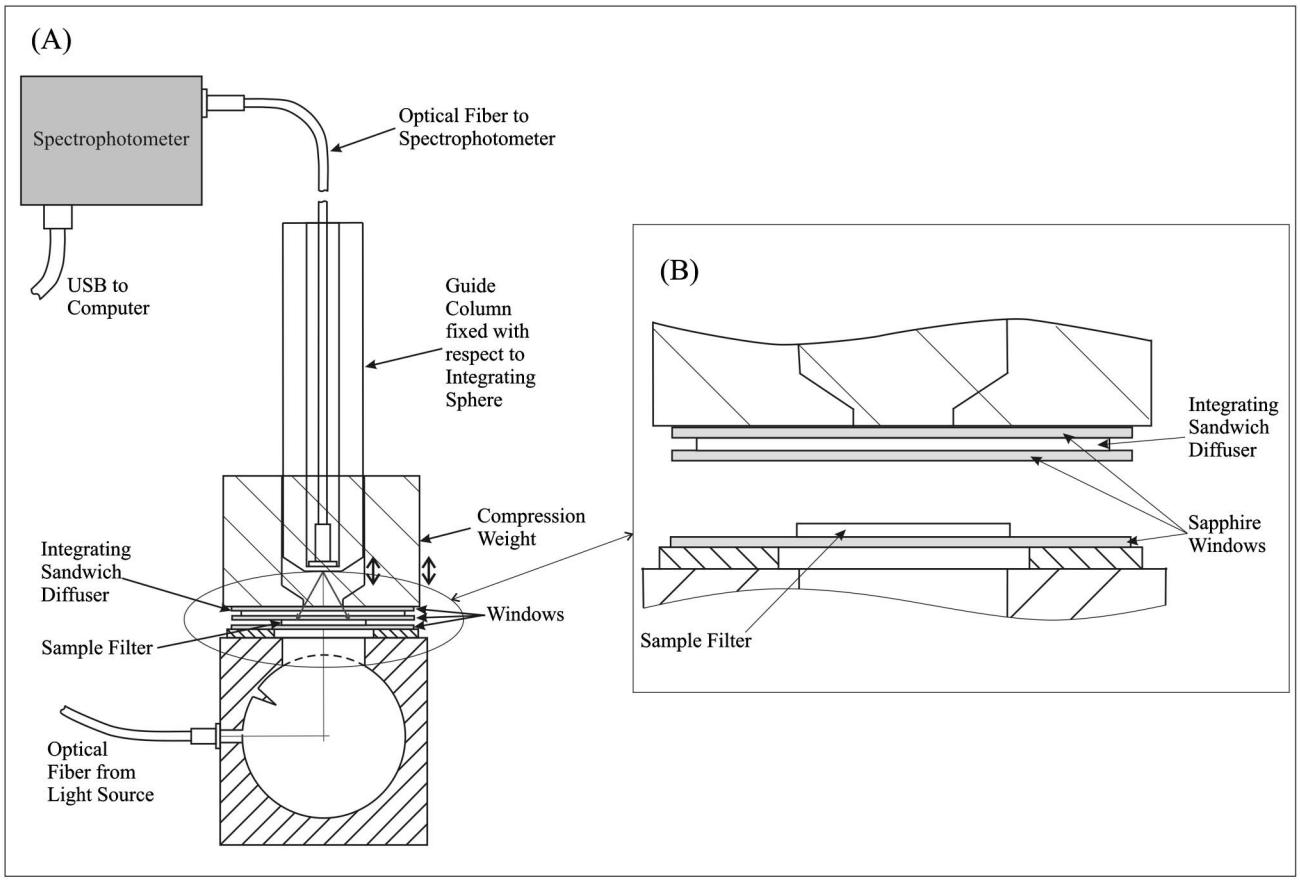

Fig. 2. (A) Schematic of ISSW spectrophotometer system optics. (B) Expanded view shows the configuration of the integrating sandwich with the compression weight raised to allow sample filter insertion.

The radiation transmitted upward through the diffuser is transmitted to an Ocean Optics Red Tide spectrophotometer, and the resulting spectrum is recorded on a laptop computer via a USB connection. A critical feature of the spectrophotometer is the presence of an order-blocking filter, which reduces the second-order spectral overlap signal by a factor 10^4 or better. The second-order spectrum would not be significant for wavelengths below 700 nm in any case, and for the present application the greatest primary intensity falls in this wavelength range, minimizing the potential effect of such light leakage. Dark-level spectral readings are measured for each sample by inserting an opaque screen into the light path and are subtracted from the signal during our data reduction procedure. The dark-level spectra showed no dependence on wavelength, indicating that the amount of external stray light entering the system was negligible. The spectrophotometer runs on 5 V DC, rather than using an AC power supply, to minimize system noise and signal drift. The spectral sensitivity is limited to the range 400–750 nm. Below 400 nm the cutoff is due to the low sensitivity of the CCD detectors compared with instrument noise, and a longwave-blocking filter mounted in the illumination unit cuts off the infrared beyond 750 nm. The available wavelength range covers most of the spectral range over which light absorption in snow and ice is predominantly affected by BC and other light-absorbing aerosols [20]. The spectral resolution of the system is approximately 2 nm across the full spectrum, providing the capability to detect molecular absorption features that may be present in different types of material collected on the filters.

4. Calibrations

Calibration of the system is based on a set of seven standard filters with a series of loadings ($L, \mu g\,cm^{-2}$) of Monarch 71, a commercially produced soot. These were prepared through sequential dilutions and gravimetric confirmation of a standard soot suspension obtained after previous filtration through 2.0 μm and 0.8 μm pore Nuclepore filters in order to remove larger particles not representative of ambient samples. Preparation of these reference filters is described in [3]. The filter loadings span a range sufficient to define the instrument sensitivity curves for field samples over the full visible spectral band of interest. Observations of the transmitted light sensed by the system for a sample, $S(\lambda)$, are compared with the signal detected for a blank filter, $S_0(\lambda)$, and the relative attenuation is expressed as

$$\chi_\lambda \equiv \ln[S_0(\lambda)/S(\lambda)]. \quad (1)$$

Specification of these and other symbols used in the text is given in Table 1. An integration time of 5.8 s

Table 1. Symbols Used in Text

Symbol	Description of Subscripts
est	Estimated; e.g., best estimate of BC level
equiv	Equivalent; based on ascribing all absorption on filter to an equivalent loading of BC
MAX	Maximum; based on assuming that all absorption from 650 to 700 nm is due to BC
NBC	Non-black-carbon component of absorption
tot	Wavelength integrated from 300 to 750 nm
Symbol	**Description of Variables**
$Å_i$	Absorption Ångstrom exponent describing the wavelength dependence of absorption by a particular type of absorber in a specified spectral range via $\tau(\lambda) \propto \lambda^{-Å}$. Index i denotes tot, BC, or NBC as required.
$\beta(\lambda)$	Mass-absorption efficiency, m^2/g. For our standard M71 soot samples $\beta(525\,nm) = 6\,m^2/g$.
τ_i^k	Absorption optical depth (dimensionless) of the material deposited onto the filter. Equal to filter loading multiplied by β, and in general depends on wavelength. Index i denotes tot, BC, or NBC as required. The index k denotes MAX or estimated (est); it is absent if i = tot.
L_{BC}^k	BC loading of filter. Index k denotes MAX, est, or equiv.
C_{BC}^k	Concentration of BC in snow. Index k denotes MAX, est, or equiv.
r_j	The ratio $\tau_j(\lambda_0)/\tau_{tot}(\lambda_0)$, where j denotes BC or NBC as indicated. Here $\lambda_0 = 525$ nm.
f_{BC}^k	The ratio of BC absorption to total absorption from 300 to 750 nm. Index k denotes MAX or est.
f_{NBC}^k	$[1 - f_{BC}^k]$. Index k denotes MIN or est.
E_{BC}^k	Maximum wavelength-integrated absorption of solar energy by BC from 300 to 750 nm. Dimensionless. Index k denotes MAX or est.
E_{TOT}	Wavelength-integrated absorption of solar energy from 300 to 750 nm by all material on filter. Dimensionless.
$S_0(\lambda)$	Detected signal for an unloaded filter, relative voltage
$S(\lambda)$	Detected signal for a loaded filter, relative voltage
χ_λ	Relative spectral attenuation, $\ln[S_0(\lambda)/S(\lambda)]$. Dimensionless.
F_{net}	Net spectral irradiance in the vicinity of the filter and integrating sandwich, W/m^2
F_s	Scalar irradiance in the vicinity of the filter and integrating sandwich, W/m^2
κ_{abs}	Volume absorption coefficient of the material deposited onto the filter for single transit of a plane wave, m^{-1}
R_1	Reflectivity of the integrating sphere-filter combination
R_2	Reflectivity of the integrating sandwich
A/M	Ratio of exposed area on filter (A, m^2) to the total mass of snow filtered (M, g).

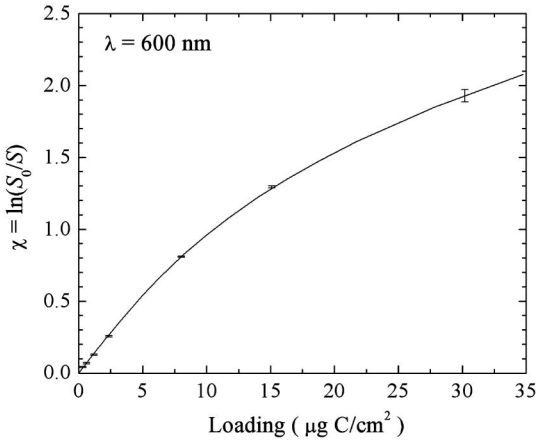

Fig. 3. Calibration curve for 600 nm wavelength relative to Monarch-71 standards. Individual points are the values from ISSW scans. The solid curve is a best-fit to the loading, L, using a third-order polynomial of the form $L = A\chi + B\chi^3$. $A = 8.689$ and $B = 1.862$

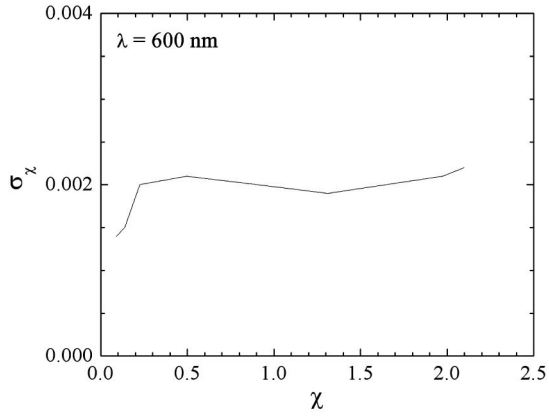

Fig. 4. Uncertainty in filter loading. Standard deviation, σ_χ, versus $\chi = \ln(S_o/S)$ at 600 nm for a series of 28 calibration runs on a set of reference filters.

has been used for both the calibration tests and processing of field samples. A representative calibration curve for 600 nm is shown in Fig. 3. Multiple filters with different loadings are needed because the system response deviates from a Beer's law exponential behavior as shown. This is a consequence of the multiple reflections produced by the integrating sandwich [18] and will be described in more detail below. A third-order polynomial fit to the calibration curve reproduces the observations to within the accuracy of the measurement, allowing us to convert measured values of χ_λ to L. Absorption optical depth is then calculated from $\tau_\lambda = L\beta_\lambda$, where β_λ is the mass-absorption efficiency for which we use $6\,m^2/g$ at 525 nm, the value for the Monarch 71 BC on the standard filters. This ensures that the radiation absorption by the sample at 525 nm is consistent with the radiation absorbed by the standard filters. The calibration sequence is repeated regularly to monitor for unexpected changes in system characteristics. For samples of pure soot, we would in principle need measurements only at a single wavelength, but since natural samples often contain other material besides BC, we can exploit spectral observations to investigate the amount of BC versus non-BC material. In this case, L is the equivalent BC mass loading that produces the correct total radiation absorption. The treatment of BC versus non-BC material is discussed in detail in Section 7.

5. Precision and Uncertainties

After a warm-up time of about 1 h, the stability of the system is approximately 0.4% over several hours of operation. A series of 28 calibrations spanning several weeks gave a standard deviation of 2.5% or less, demonstrating the long-term system stability. Representative results at 600 nm are shown in Fig. 4. The short-term stability of the calibration over individual tests lasting several hours was 0.2%.

The percentage uncertainty in derived loading at a wavelength of 600 nm is shown in Fig. 5(a) as a function of loading. The noise-to-signal ratio for filter loading is optimal near $2\,\mu g/cm^2$ with a range of good performance of better than ~7% from about 0.2 to $6\,\mu g/cm^2$. For L values outside this range the signal levels decrease significantly relative to system noise. For L values near the optimum value, the accuracy for an individual sample is about 2%. The corresponding uncertainty versus wavelength for a representative value of $L = 2\,\mu g/cm^2$ is shown in Fig. 5(b). The uncertainty is ~2% from 490 to 730 nm and is less than 5% between 420 and 740 nm. In practice, we exclude wavelengths longer than 750 nm to conform to the band over which background levels of light-absorbing aerosol absorption are significant for snow. These results show that the optimal volume of snow for a sample is that which gives a filter loading of $1–3\,\mu g/cm^2$. It is not possible to know the precise volume needed *a priori* at a new site since the required volume increases for cleaner snow; but near-optimal results can be obtained iteratively by visually examining the darkness of the initial filters and resampling with an adjusted volume of snow.

Uncertainty in ISSW measurements arises not only from instrumental uncertainties but also from nonuniformities in the aerosol deposition on the filter. In addition, filters occasionally shifted partially out of the fiber-optic field of view when lowering the compression weight. For this reason, we made two measurements for each sample filter, repositioning it in the sample cell between the two measurements. Generally the difference between the two measurements was in the range 0%–4%, and the average value is recorded. Where the difference was 10% or more, subsequent repeat measurements were made. If agreement to better than 10% between multiple additional measurements was obtained, the result was included in the data set; otherwise the sample was excluded. Less than 1% of field samples were excluded, and in each of these cases the filter exposure was nonuniform. This type of error does not depend

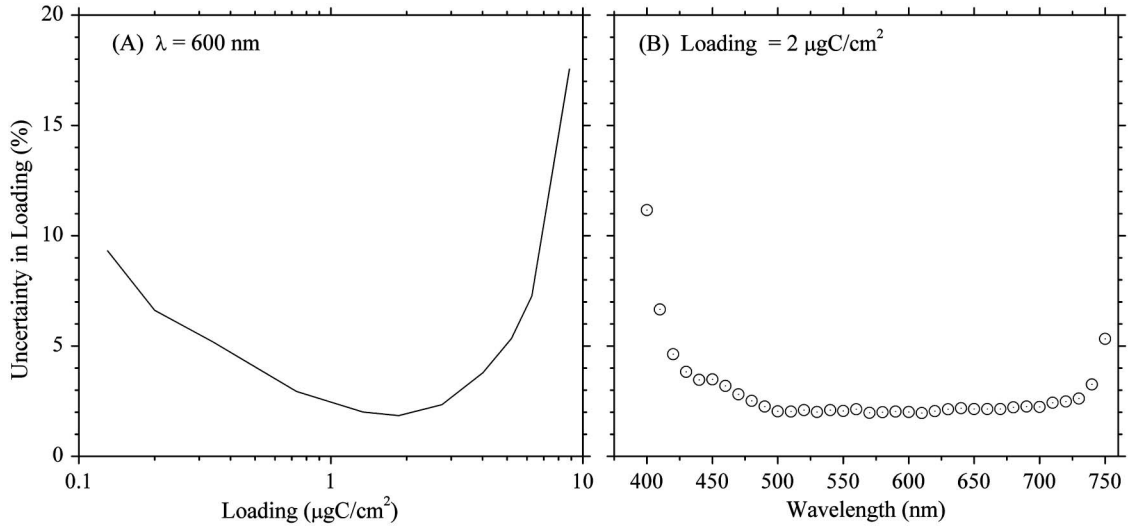

Fig. 5. Percent uncertainty in loading, $\frac{100}{L}\frac{\partial L}{\partial \chi}\sigma_\chi$, for an ensemble of 28 calibration runs versus (A) filter loading at 600 nm and (B) wavelength for a loading of $2\,\mu$gC/cm^2. The optimal spectral range is from 420 to 740 nm.

on the performance characteristics of the ISSW system.

6. Theory

Because of the highly diffuse radiation field in the sample cavity, the integrating-sandwich method lends itself to analysis using a straightforward transformation of the flux integral {Eq. (56) in [21]}, alternatively known as Gershun's law ([22], p. 423). This is a rigorous result based on the equation of radiative transfer for an arbitrary plane parallel scattering and absorbing medium that isolates the absorption coefficient:

$$\frac{dF_{\text{net}}}{dz} = -\kappa_{\text{abs}} F_s, \tag{2}$$

where F_{net} is the net irradiance and κ_{abs} is the volume absorption coefficient. F_s is the scalar irradiance [23,24], 4π times the mean radiance. Since the radiation field interacting with the sample filter in the cavity between the integrating sphere and the diffusing sandwich is diffuse, we assume that the radiation field is isotropic in both the forward and backward hemispheres at the location of the filter. With this assumption, the solution of the flux integral can be derived by the same method used for the discrete ordinates method. The derivation is given in the Appendix. The ratio of detected signal intensity, S, at a particular wavelength for a loaded filter compared with that of a reference blank is shown to be

$$\frac{S}{S_0} = \exp(-2\tau)\frac{1 - R_1R_2}{1 - R_1R_2\exp(-4\tau)}, \tag{3}$$

where R_1 and R_2 are the reflectivities of the integrating-sphere/filter combination and the integrating-sandwich diffuser, respectively, and τ is the total absorption optical depth for the material on the filter. Rather than using the thickness of the collected material, we measure L_{BC} for each sample by comparison with the standard filters, and the absorption optical depth is given by the more convenient quantity $\tau = L \cdot \beta_\lambda$, which is equal to $\int \kappa_{\text{abs}} dz$.

Equation (3) is essentially an exact solution for the instrument, subject only to the assumption of hemispherical isotropy and the approximation of plane-parallel geometry at the filter location. Inverting and taking the logarithm, we obtain

$$\chi_\lambda = 2\tau + \ln\frac{[1 - R_1R_2\exp(-4\tau)]}{[1 - R_1R_2]}. \tag{4}$$

The first factor in Eq. (4) shows that there is an enhancement of absorption by a factor of 2 over a beam transmission measurement (2 is the mean secant of a diffuse radiation field). The second factor describes the additional absorption produced by multiple passes of the radiation through the filter due to reflections in the integrating chamber.

The system response is independent of scattering by the material on the filter. Although scattering losses by BC are expected to be small compared with absorption, non-BC material can contribute significant scattering losses when using an apparatus that does not have a truly isotropic radiation field. The ISSW instrument essentially removes the influence of all scattering losses from the system. The denominator of the second term in Eq. (3) indicates that the response of the system is nonexponential as seen in Fig. 3. The system sensitivity is related to the slope of this curve and is greatest for very small values of loading, reaching an asymptotic value for large τ.

For the present configuration, the lowest useful values of L are approximately $0.2\,\mu$g/cm^2. For values of L above about $6\,\mu$g/cm^2, the transmitted radiation will be attenuated below levels where system noise again begins to dominate. As mentioned above,

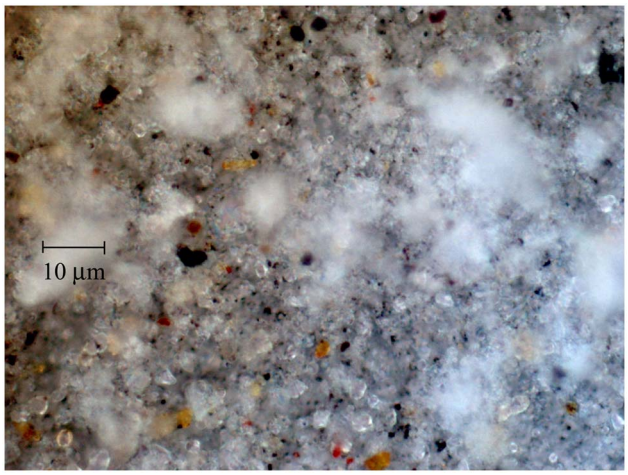

Fig. 6. (Color online) Optical microscope image of filter sample from snow in northern Canada, May 2009, showing black soot conglomerates and red-brown dust particles. Smallest visible detail is ~0.2 μm. Courtesy of Professor Don Brownlee (University of Washington, Department of Astronomy).

exceeding these limits can be avoided by resampling the snow to adjust the volumes of meltwater filtered.

7. Separation of the Contributions to Absorption by Black Carbon and non-Black-Carbon Absorbers

In addition to BC, snow often contains other light-absorbing aerosols such as soil dust and organic carbon. These are often brown or reddish-brown. An optical-microscope photograph of an example from snow in Canada is shown in Fig. 6 in which many colored dust particles are visible. To understand the spectral absorption of light in a snowpack it is important to distinguish between particles consisting of pure BC and other colored particulates that we refer to here collectively as non-BC particles. The effect of the latter on the ISSW scans is to alter the spectral shape of the absorption curves and the resulting total absorption. This effect has been described previously [3,25,26].

Because the ISSW instrument provides 2 nm spectral resolution, it offers the potential to determine separately the contributions of BC and non-BC aerosols to the total absorption. The dependence of absorption optical depth on wavelength is often characterized by a power law, $\tau(\lambda) \propto \lambda^{-\text{Å}}$, over a particular wavelength range of interest, where Å is called the Ångstrom exponent. For BC, the value of Å is very close to 1 for visible wavelengths, and the values for non-BC aerosols are significantly larger [27–29]. We take advantage of these differences in spectral shape as described below. Non-BC light-absorbing components have been identified and characterized as brown carbon [30,31], organic carbon [32], and soil dust [33]. Brown sediments have also been found in samples of sea ice and its snow cover [16].

A. Upper Limit to Black Carbon

As an initial limiting approximation, we determine an estimated upper bound to the contribution of BC to absorption of solar radiation by assuming that all absorption from 650 to 700 nm is due to BC, with an absorption optical depth $\tau_{\text{BC}}^{\text{MAX}}$. The filter loading, $L_{\text{BC}}^{\text{MAX}}$, is derived from the calibration against the standard samples over the 650–700 nm interval. The corresponding BC concentration in the snow is given by

$$C_{\text{BC}}^{\text{MAX}} = L_{\text{BC}}^{\text{MAX}} \cdot (A/M), \tag{5}$$

where M is the mass of meltwater filtered and A is the exposed area on the filter. This gives a value of nanograms of BC per gram of snow meltwater or, equivalently, ppb. To determine $\tau_{\text{BC}}^{\text{MAX}}$ we multiply $L_{\text{BC}}^{\text{MAX}}$ by a mass-absorption efficiency, $\beta(\lambda)$, obtained by scaling the value of 6 m^2/g at 525 nm and extrapolating to 675 nm, using an Ångstrom exponent of 1.0 as specified above. Values of $\beta(\lambda)$ for a set of calibration filters using a different type of soot may differ from this, in which case $\beta(\lambda)$ should reflect the optical properties of the chosen calibration material.

Using the spectral dependence of the measured light absorption offers the potential to obtain additional information about other material that may be present in the snow. A representative case is shown in Fig. 7. After specifying $\tau_{\text{BC}}^{\text{MAX}}$, the BC spectral curve (dashed line) is calculated by extrapolating from the 650–700 nm band over the range 300 to 750 nm again using an Ångstrom exponent of 1. This wavelength interval has been chosen because solar radiation at the surface is negligible below 300 nm, and impurities have little effect on snow albedo for $\lambda > 750$ nm. We use the measured absorption over the 420–700 nm interval where the signal-to-noise ratio is optimized. The total absorption curve is extended over the full spectral range by linear extrapolation from 420 to 300 nm and from 700 to 750 nm. The extrapolations are carried out using the mean

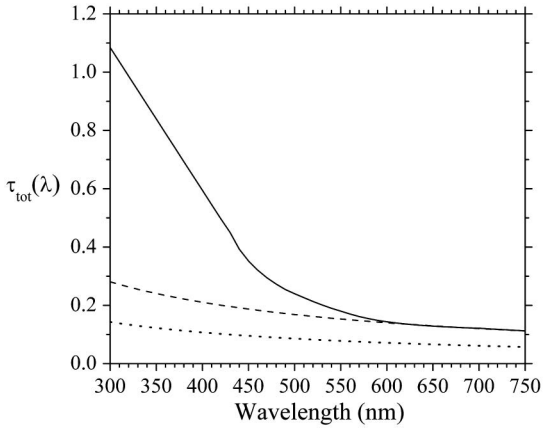

Fig. 7. Absorption optical depth versus wavelength for a sample filter containing BC and non-BC components from a snow sample from the Canadian Arctic in spring 2009. The solid line shows total absorption optical depth, and the dashed curve gives the maximum BC contribution assuming that all absorption at 650–700 nm is due to BC and that $\text{Å}_{\text{BC}} = 1.0$. The dotted curve gives the estimated BC absorption using Eqs. (9) and (10) assuming $\text{Å}_{\text{NBC}} = 5$.

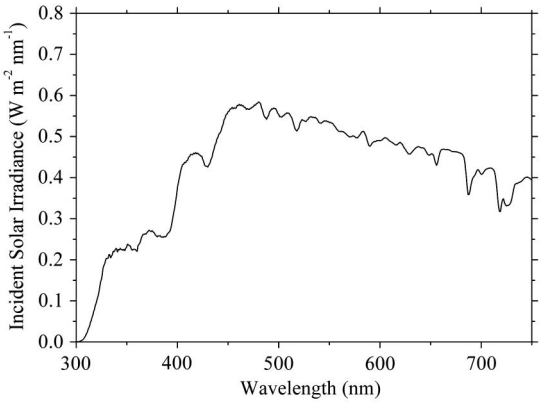

Fig. 8. Incident solar irradiance, $F_o(\lambda)$, from the Arctic summer (2005) in the northern Beaufort Sea for a relatively clear day with some light clouds and fog [34]. The wavelength range is limited to the 300–750 nm band used for the absorption calculations. The spectrum has been extended from 350 to 300 nm using the SBDART model [35] using the subarctic summer atmospheric profile.

slope of the absorption curve in the range 420 to 450 nm for the ultraviolet wavelengths, and the mean slope in the range 630–700 nm is used for the near infrared. To obtain the relative contributions of the estimates of BC and non-BC material to the absorption of solar energy over the entire solar spectrum, the total and extrapolated absorption curves are weighted by the incident spectral irradiance, $F_o(\lambda)$.

The solar spectrum used here and shown in Fig. 8 is an example from summer in the Arctic Basin [34] extended to 300 nm using the SBDART model [35] using the subarctic summer atmospheric profile. The weighted curves (Fig. 9) are then integrated over wavelength as follows to give the wavelength-integrated relative absorption by all the material on the filter (E_{TOT}) and by BC ($E_{\mathrm{BC}}^{\mathrm{MAX}}$):

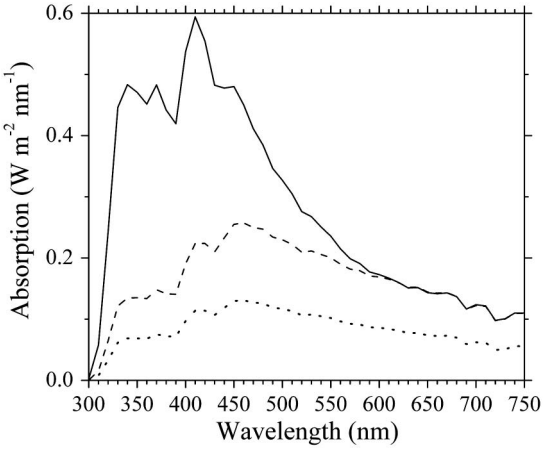

Fig. 9. Spectral absorption, $F_o(\lambda)\tau(\lambda)$, for a site in the Canadian Arctic in 2009 for all constituents (solid line), maximum BC (dashed line), and estimated BC (solid line) using the same Å values as for Fig. 8.

$$E_{\mathrm{TOT}} = \frac{\int_{300}^{750} F_o(\lambda)\tau_{\mathrm{TOT}}(\lambda)\mathrm{d}\lambda}{\int_{300}^{750} F_o(\lambda)\mathrm{d}\lambda},$$
$$E_{\mathrm{BC}}^{\mathrm{MAX}} = \frac{\int_{300}^{750} F_o(\lambda)\tau_{\mathrm{BC}}^{\mathrm{MAX}}(\lambda)\mathrm{d}\lambda}{\int_{300}^{750} F_o(\lambda)\mathrm{d}\lambda}. \quad (6)$$

The estimated upper bound of fractional absorption for BC and the corresponding minimum for non-BC are given by the ratios

$$f_{\mathrm{BC}}^{\mathrm{MAX}} = E_{\mathrm{BC}}^{\mathrm{MAX}}/E_{\mathrm{tot}}, \quad f_{\mathrm{NBC}}^{\mathrm{MIN}} = 1 - f_{\mathrm{BC}}^{\mathrm{MAX}}. \quad (7)$$

An advantage of this technique is that no assumption is necessary concerning the Ångstrom exponent for the non-BC material; however, this technique provides only a lower limit to the absorption by non-BC because non-BC absorption is not negligible at 650–700 nm in general.

B. Estimated Black Carbon

Our best estimate of the actual amount of BC and non-BC material on the filter is obtained by exploiting differences in the Ångstrom exponents for BC and non-BC components. From the measured absorption spectrum using $\tau_{\mathrm{tot}}(\lambda)$ specified as described above, we compute the Ångstrom exponent, Å_{tot}, that describes the wavelength dependence of the absorption optical depth for all the material deposited on a particular filter in the neighborhood of a reference wavelength λ_0. The exponent is calculated from the shape of the total absorption curve (e.g., solid curve in Fig. 7) using the logarithmic formula

$$\text{Å}_{\mathrm{tot}}(\lambda_0) = \frac{\ln[\tau_{\mathrm{tot}}(\lambda_1)/\tau_{\mathrm{tot}}(\lambda_2)]}{\ln[\lambda_2/\lambda_1]}, \quad (8)$$

where we have used values of 525, 450, and 600 nm for λ_0, λ_1, and λ_2, respectively We can express $\text{Å}_{\mathrm{tot}}(\lambda_0)$ in terms of the BC and non-BC components as follows:

$$\tau_{\mathrm{tot}}(\lambda_0)\cdot\left(\frac{\lambda}{\lambda_0}\right)^{-\text{Å}_{\mathrm{tot}}} = \tau_{\mathrm{BC}}(\lambda_0)\cdot\left(\frac{\lambda}{\lambda_0}\right)^{-\text{Å}_{\mathrm{BC}}} + \tau_{\mathrm{NBC}}(\lambda_0)\cdot\left(\frac{\lambda}{\lambda_0}\right)^{-\text{Å}_{\mathrm{NBC}}}, \quad (9)$$

where Å_{BC} and Å_{NBC} are the Ångstrom exponents for BC and non-BC specified at λ_0. If we define r_{BC} and r_{NBC} to be the ratios $\tau_{\mathrm{BC}}(\lambda_0)/\tau_{\mathrm{tot}}(\lambda_0)$ and $\tau_{\mathrm{NBC}}(\lambda_0)/\tau_{\mathrm{tot}}(\lambda_0)$, respectively, then in a neighborhood around λ_0 we can show via Taylor series expansion, for example, that

$$\text{Å}_{\mathrm{tot}} = \text{Å}_{\mathrm{BC}} r_{\mathrm{BC}}(\lambda_0) + \text{Å}_{\mathrm{NBC}}(1 - r_{\mathrm{BC}}(\lambda_0)), \quad (10)$$

where $r_{\mathrm{NBC}} = 1 - r_{\mathrm{BC}}$. So Å_{tot} is a linear combination of the exponents for BC and non-BC weighted by the absorption fraction of each type of absorber, and it

can be determined directly from an observed spectral absorption curve using Eq. (8). Thus, if we have independent knowledge of Å_{BC} and Å_{NBC} over a wavelength interval of 100–150 nm about λ_0, for example, then $r_{\text{BC}}(\lambda_0)$ is given by Eq. (10). For our analysis we assume that $\text{Å}_{\text{BC}} = 1.0$. A value of 5 was chosen for Å_{NBC}, consistent with Ångstrom coefficients reported in the range 4 to 6 for the "brown carbon" component of biomass-burning aerosol [31] and with values inferred from spectral absorption measurements of organic-carbon aerosols (Table 4 of [32]). For Å_{NBC} lower than about 4.5 nonphysical values (estimated BC concentrations of less than 0) resulted for some samples. Values of Å_{tot} fall between Å_{BC} and Å_{NBC} [36] as per Eq. (10).

The estimated absorption optical depth of BC,

$$\tau_{\text{BC}}^{\text{est}}(\lambda_0) = r_{\text{BC}}(\lambda_0) \cdot \tau_{\text{tot}}(\lambda_0), \tag{11}$$

is then scaled across the spectrum via

$$\tau_{\text{BC}}^{\text{est}}(\lambda) = \tau_{\text{BC}}^{\text{est}}(\lambda_0)(\lambda/\lambda_0)^{-\text{Å}_{\text{BC}}} = \tau_{\text{BC}}^{\text{est}}(\lambda_0)(\lambda_0/\lambda), \tag{12}$$

as shown by the dotted line in Fig. 7, and the estimated BC loading is given by

$$L_{\text{BC}}^{\text{est}} = [L_{\text{BC}}^{\text{MAX}} \cdot \langle \tau_{\text{BC}}^{\text{est}} \rangle_{650\text{–}700} / \langle \tau_{\text{BC}}^{\text{MAX}} \rangle_{650\text{–}700}]. \tag{13}$$

The spectrally integrated fractions of absorption by BC, $f_{\text{BC}}^{\text{est}}$, and by non-BC constituents, $f_{\text{NBC}}^{\text{est}} = [1 - f_{\text{BC}}^{\text{est}}]$, are obtained from Eqs. (6) and (7) substituting $\tau_{\text{BC}}^{\text{est}}(\lambda)$ for $\tau_{\text{BC}}^{\text{MAX}}(\lambda)$. The estimated concentration of BC in snow, $C_{\text{BC}}^{\text{est}}$, is derived from the loading on the filter, $L_{\text{BC}}^{\text{est}}$, as in Eq. (5).

The main limitation of this method is the accuracy to which we know the value of Å_{NBC} in the vicinity of λ_0; however, even if Å_{NBC} is not well known, Å_{tot}, which is measured directly, is important *per se* to help provide a general characterization of the samples. Results are included in Figs. 7 and 9 assuming that Å_{NBC} at that site is 5.0. In the Arctic, the absorption by the non-BC component is highly correlated with the biomass-burning source factors [37], which indicates a preponderance of brown carbon as opposed to dust. A chemical analysis profile is clearly desirable in conjunction with the ISSW observations to help specify the nature of the non-BC fraction. If Å_{NBC} is less than (greater than) 5, our derived BC amounts would be biased high (low).

C. Equivalent Black Carbon

Models that do not distinguish the various impurities in snow may represent the effect of all absorbers by the amount of BC needed to explain the total absorption. We therefore also report this quantity for our analyses of filter loading, which we call "equivalent BC." It is determined by the ratio of the integrals of the total and estimated spectral absorption curves (Fig. 9):

$$L_{\text{BC}}^{\text{equiv}} = L_{\text{BC}}^{\text{est}} \frac{\int_{300}^{750} F_o(\lambda)\, \tau_{\text{TOT}}(\lambda)\, \mathrm{d}\lambda}{\int_{300}^{750} F_o(\lambda)\, \tau_{\text{BC}}^{\text{est}}(\lambda)\, \mathrm{d}\lambda} = \frac{L_{\text{BC}}^{\text{est}}}{f_{\text{BC}}^{\text{est}}}, \tag{14}$$

$$C_{\text{BC}}^{\text{equiv}} = C_{\text{BC}}^{\text{est}} / f_{\text{BC}}^{\text{est}}. \tag{15}$$

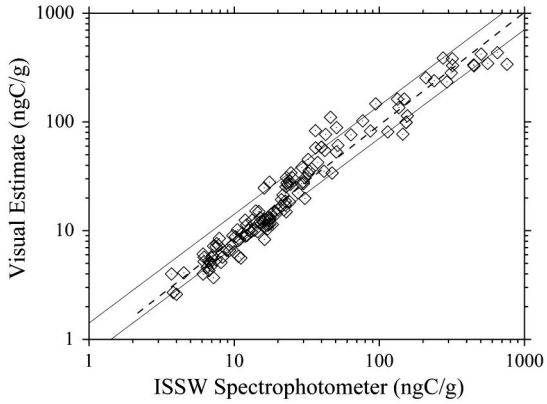

Fig. 10. Comparison of equivalent concentration, $C_{\text{BC}}^{\text{equiv}}$ determined by the ISSW spectrophotometer from Eqs. (14) and (15), versus the values from visual estimates for samples of snow from the Russian Arctic in 2007, for which the non-BC levels were low. The upper and lower lines show the limits of a factor of 2 variation about the line of perfect agreement. Linear regression in ln-ln space, the dashed curve, gives $\ln[C(\text{Visual})] = \{1.038 * \ln[C(\text{ISSW})] - 0.2432\}$ with a correlation coefficient of 0.973 and a standard error of 0.300.

8. Comparison of ISSW Results with Visual Absorption Estimates

Since some published results were obtained using visual comparison against our set of standard filters [15,16], it is important to know how well these estimates compare with spectrophotometer results. The visual comparison gives an estimate of the equivalent BC concentration ($C_{\text{BC}}^{\text{equiv}}$), which is the amount of BC that would be needed to explain the total filter darkening including both BC and non-BC components. The visual comparisons are made by comparing the filter loading contrast relative to the standards between the exposed area of each filter and its unexposed outer edge and then applying Eq. (5) with superscript *MAX* replaced by *equiv*.

Figure 10 shows a comparison of equivalent BC concentration with visual estimates spanning a range of about 200 for snow samples from one expedition. Departures from the ISSW values lie within bounds of uncertainty that span a factor of 2. The linear regression curve in $\log(C_{\text{vis}}) - \log(C_{\text{ISSW}})$ space is shown. The coefficient of correlation is 0.973 with a standard error of 0.300, which is less than $\ln(\sqrt{2}) = 0.346$. There is good agreement to within a factor of approximately $\sqrt{2}$. There is a slight low bias particularly evident for low concentrations likely due to personal bias of the observer. The error

in the visual comparisons is small compared with naturally occurring temporal [12] and spatial [3] variations of BC, so the visual estimates provide useful information; however, the ISSW instrument improves the precision by a factor of ~70.

9. Conclusions

A new spectrophotometric instrument for measuring the absorption properties of light-absorbing aerosols present in ice and snow based on the integrating-sandwich principle has been constructed, taking advantage of recent developments in optical component technology. The short-term stability is ~0.4%, and the long-term stability for a series of 28 measurements spanning several weeks is better than 2.5%. Calibrations against a set of filters of known BC loading have shown that the relative accuracy in loading ranges from 2% to 5% over the spectral range 420–740 nm for loading near 1 μgC/cm^2. Theoretical analysis based on the flux integral of radiative transfer provides a quantitative measure of the sensitivity enhancement over the integrating-plate photometer technique. It demonstrates the capability of the integrating-sandwich configuration to isolate the absorption properties of material deposited on polycarbonate Nuclepore filters, essentially eliminating the effect of losses due to volume-scattering by absorbing and nonabsorbing particulate material in or on the filter. This advantage far outweighs the disadvantage of the strong light attenuation introduced by the integrating-sandwich configuration. Using the assumption that all 650–700 nm light absorption is due to BC, we derive the maximum concentration of BC in the snow and the minimum contribution to absorption by other aerosol by comparing wavelength integrals of total and BC absorption of solar radiation. We also determine an Ångstrom exponent for all light-absorbing aerosol in the sample to further characterize each sample. By combining Å_{tot} with an estimate for the absorption Ångstrom exponent for BC and non-BC aerosols, the method is extended to give values of the actual BC concentrations and fractional absorption of visible and near-UV solar radiation due to the non-BC aerosol.

We have used the ISSW instrument specifically to quantify BC and non-BC contributions to light absorption in snow; however, the instrument and the analysis described here can be used for identification of other types of light-absorbing aerosol. This would require recalibration using a set of standards for the materials of interest in conjunction with the use of the appropriate spectral signatures to separate the contributions from the different absorbers.

Appendix A: Derivation of Eq. (4)

Considering the radiation field in the vicinity of the sample filter (Fig. 2), we assume that a plane-parallel representation provides an accurate description near the filters, since the radiation field is highly homogeneous there. We define three regions to be considered where we specify the boundary conditions for the problem. Region 1 is the cavity volume below the material on the filter. Region 2 is the cavity volume above the filter and below the integrating sandwich, including the material deposited on the filter. Region 3 is the volume above the integrating sandwich from which the radiation is transmitted to the detector by the optical fiber. We divide the integrals for irradiance in Gershun's law into separate components for the upward and downward hemispheres:

$$F_{\text{net}} = \int_0^{2\pi}\int_0^1 \mu I(\mu,\phi)\mathrm{d}\mu\mathrm{d}\phi + \int_0^{2\pi}\int_{-1}^0 \mu I(\mu,\phi)\mathrm{d}\mu\mathrm{d}\phi, \tag{A1}$$

$$F_s = \int_0^{2\pi}\int_0^1 I(\mu,\phi)\mathrm{d}\mu\mathrm{d}\phi + \int_0^{2\pi}\int_{-1}^0 I(\mu,\phi)\mathrm{d}\mu\mathrm{d}\phi, \tag{A2}$$

where $I(\mu,\phi)$ is the radiance, μ is the cosine of the polar angle, and ϕ is the azimuth angle, standard definitions in radiative transfer theory [21]. The radiance in the vicinity of the filter is highly diffuse and assumed to be separately isotropic in both hemispheres. In this case, the radiance can be expressed as $I(\pm) = F_+/\pi$ or F_-/π in the upward and downward hemispheres, respectively. Then we obtain

$$F_{\text{net}} = F_+ - F_-, \tag{A3}$$

$$F_s = 2(F_+ + F_-). \tag{A4}$$

Gershun's law [Eq. (2)] can then be expressed as

$$\frac{d(F_+ - F_-)}{d\tau} = -2(F_+ + F_-), \tag{A5}$$

where $d\tau = \kappa_{\text{abs}} \cdot dz$ is the formal definition of differential absorption optical depth, and the total absorption optical depth of material on the filter is $\tau = \int \kappa_{\text{abs}} \cdot \mathrm{d}z$. We have the following boundary conditions: in region 1

$$F_+(1) = F_0 + R_1 \cdot F_-(1), \tag{A6}$$

in region 2

$$F_-(2) = R_2 \cdot F_+(2), \tag{A7}$$

and in region 3

$$F_+(3) = (1 - R_2) \cdot F_+(2). \tag{A8}$$

F_o denotes the direct contribution to $F_+(1)$ from the light source. Its value is not needed because it cancels out of the final solution needed here. If the field of view of the optical fiber detector is Ω_d, then the detected signal, S, is proportional to $\Omega_d F_+(3)$.

Following the techniques of Chandrasekhar [21], we seek solutions of (A5) of the form

$$F_l = g_l \cdot \exp(k_l \cdot \tau), \tag{A9}$$

where l denotes + or −; k_l are coefficients related to the absorption properties of the aerosol on the filter and are specified by the form of (A5); and g_l are integration constants for (A5) to be specified by the boundary conditions (A6) through (A8). Substituting into (A5) and collecting terms, we obtain the characteristic equation for (A5):

$$(k_+ g_+ + 2g_+)\exp(k_+\tau) + (-k_- g_- + 2g_-)\exp(k_-\tau) = 0. \tag{A10}$$

For (A10) to hold for an arbitrary value of τ, the coefficients of each exponential term must separately be zero giving

$$k_+ = -2, \quad k_- = 2, \tag{A11}$$

so

$$F_+ = g_+ \exp(-2\tau), \quad F_- = g_- \exp(2\tau). \tag{A12}$$

Substituting these into the boundary conditions (A6) and (A7) noting that $\tau(1) = 0$ and $\tau(2) = \tau$, the absorption optical depth of material on a filter, we have

$$g_+ = F_0 + R_1 g_-, \tag{A13}$$

$$g_- \exp(2\tau) = R_2 g_+ \exp(-2\tau). \tag{A14}$$

These give

$$g_+ = \frac{F_0}{1 - R_1 R_2 \exp(-4\tau)}, \quad g_- = \frac{R_2 \exp(-4\tau) F_0}{1 - R_1 R_2 \exp(-4\tau)}. \tag{A15}$$

So

$$F_+ = \frac{F_0}{1 - R_1 R_2 \exp(-4\tau)} \exp(-2\tau),$$
$$F_- = \frac{R_2 \exp(-2\tau) F_0}{1 - R_1 R_2 \exp(-4\tau)}. \tag{A16}$$

We assume that absorption by the optical components of the system is negligible, although the final results are still rigorous even if a small constant amount of absorption is present. Then from (A8) the detected signal, S, for a loaded filter is

$$S = \Omega_d F_+(3) = \frac{\Omega_d F_0 (1 - R_2)}{1 - R_1 R_2 \exp(-4\tau)} \exp(-2\tau). \tag{A17a}$$

For a blank filter the signal, S_0, is

$$S_0 = \frac{\Omega_d F_0 (1 - R_2)}{1 - R_1 R_2}. \tag{A17b}$$

The ratio then gives the required result

$$\frac{S}{S_0} = \exp(-2\tau) \frac{1 - R_1 R_2}{1 - R_1 R_2 \exp(-4\tau)}. \tag{A18}$$

We thank Richard Brandt for useful suggestions and help with the photometer design and Tom Ackerman for discussions on the separation of BC and non-BC contributions. Angel Adames and Hugo Froyland provided helpful suggestions based on their use of the photometer to process filters. We thank Don Brownlee for optical microscopy of the filters (Figs. 1 and 6). Two reviewers provided helpful suggestions to clarify the presentation. The research was supported by the National Science Foundation (NSF) grant ARC-06-12636.

References

1. T. C. Bond, D. G. Streets, K. F. Yarber, S. M. Nelson, J. H. Woo, and Z. Klimont, "A technology-based global inventory of black and organic carbon emissions from combustion," J. Geophys. Res. **109**, D14203 (2004).
2. T. C. Bond and R. W. Bergstrom, "Light absorption by carbonaceous particles: an investigative review," Aerosol Sci. Technol. **40**, 27–67 (2006).
3. A. D. Clarke and K. J. Noone, "Soot in the Arctic snowpack: a cause for perturbations in radiative transfer," Atmos. Environ. **19**, 2045–2053 (1985).
4. J. Hansen and L. Nazarenko, "Soot climate forcing via snow and ice albedos," Proc. Natl. Acad. Sci. USA **101**, 423–428 (2004).
5. J. Hansen, M. Sato, R. Ruedy, L. Nazarenko, A. Lacis, G. A. Schmidt, G. Russell, I. Aleinov, M. Bauer, S. Bauer, N. Bell, B. Cairns, V. Canuto, M. Chandler, Y. Cheng, A. Del Genio, G. Faluvegi, E. Fleming, A. Friend, T. Hall, C. Jackman, M. Kelley, N. Kiang, D. Koch, J. Lean, J. Lerner, K. Lo, S. Menon, R. Miller, P. Minnis, T. Novakov, V. Oinas, Ja. Perlwitz, Ju. Perlwitz, D. Rind, A. Romanou, D. Shindell, P. Stone, S. Sun, N. Tausnev, D. Thresher, B. Wielicki, T. Wong, M. Yao, and S. Zhang, "Efficacy of climate forcings," J. Geophys. Res. **110**, D18104 (2005).
6. M. G. Flanner, C. S. Zender, J. T. Randerson, and P. J. Rasch, "Present-day climate forcing and response from black carbon in snow," J. Geophys. Res. **112**, D11202 (2007).
7. P. Boparai, J. Lee, and T. C. Bond, "Revisiting thermal-optical analyses of carbonaceous aerosol using a physical model," Aerosol Sci. Technol. **42**, 930–948 (2008).
8. J. G. Slowik, E. S. Cross, J.-H. Han, P. Davidovits, T. B. Onasch, J. T. Jayne, L. R. Williams, M. R. Canagaratna, D. R. Worsnop, R. K. Chakrabarty, H. Moosmüller, W. P. Arnott, J. P. Schwartz, R.-S. Gao, D. W. Fahey, G. L. Kok, and A. Petzold, "An inter-comparison of instruments measuring black carbon content of soot particles," Aerosol Sci. Technol. **41**, 295–314 (2007).
9. E. S. Cross, T. B. Onasch, A. Ahern, W. Wrobel, J. G. Slowik, J. Olfert, D. A. Lack, P. Massoli, C. D. Cappa, J. Schwartz, R. Spackman, D. W. Fahey, A. Sedlacek, A. Trimborn, J. T. Jayne, A. Freedman, L. R. Williams, N. L. Ng, C. Mazzoleni, M. Dubey, B. Brem, G. Kok, R. Subramanian, S. Freitag, A. Clarke, D. Thornhill, L. Marr, C. E. Kolb, D. R. Worsnop, and P. Davidovits, "Soot particle studies—instrument

inter-comparison—project overview," Aerosol Sci. Technol. **44**, 592–611 (2010).
10. G. S. W. Hagler, M. H. Bergin, E. A. Smith, and J. E. Dibb, "A summer time series of particulate carbon in the air and snow at Summit, Greenland," J. Geophys. Res. **112**, D21309 (2007).
11. S. Forsström, J. Ström, C. A. Pedersen, E. Isaksson, and S. Gerland, "Elemental carbon distribution in Svalbard snow," J. Geophys. Res. **114**, D19112 (2009).
12. J. R. McConnell, R. Edwards, G. L. Kok, M. G. Flanner, C. S. Zender, E. S. Saltzman, J. R. Banta, D. R. Pasteris, M. M. Carter, and J. D. W. Kahl, "20th century industrial black carbon emissions altered Arctic climate forcing," Science **317**, 1381–1384 (2007).
13. T. C. Bond, T. L. Anderson, and D. Campbell, "Calibration and intercomparison of filter-based measurements of visible light absorption by aerosols," Aerosol Sci. Technol. **30**, 582–600 (1999).
14. T. C. Grenfell, D. K. Perovich, and J. A. Ogren, "Spectral albedos of an alpine snowpack," Cold Reg. Sci. Technol. **4**, 121–127 (1981).
15. T. C. Grenfell, B. Light, and M. Sturm, "Spatial distribution and radiative effects of soot in the snow and sea ice during the SHEBA experiment," J. Geophys. Res. **107**, 8032–8038 (2002).
16. D. K. Perovich, T. C. Grenfell, B. Light, B. C. Elder, J. Harbeck, C. Polashenski, W. B. Tucker III, and C. Stelmach, "Transpolar observations of the morphological properties of Arctic sea ice," J. Geophys. Res. **114**, C00A04 (2009).
17. A. D. Clarke, "Effects of filter internal reflection coefficient on light absorption measurements made using the integrating plate method," Appl. Opt. **21**, 3021–3031 (1982).
18. A. D. Clarke, "Integrating sandwich: a new method of measurement of the light absorption coefficient for atmospheric particles," Appl. Opt. **21**, 3011–3020 (1982).
19. A. D. Clarke, K. J. Noone, J. Heintzenberg, S. G. Warren, and D. S. Covert, "Aerosol light absorption measurement techniques: analysis and intercomparisons," Atmosph. Environ. **21**, 1455–1465 (1987).
20. S. G. Warren and W. J. Wiscombe, "A model for the spectral albedo of snow. II. snow containing atmospheric aerosols," J. Atmos. Sci. **37**, 2734–2745 (1980).
21. S. Chandrasekhar, *Radiative Transfer* (Dover, 1960).
22. A. A. Gershun, "Presentation of the fundamental ideas of the theory of a radiation field (vector methods of photometric calculation)," Izvestiya Akad. Nauk SSSR, **N 3**, 417–430 (1936) [in Russian, Proc. Acad. Sciences USSR].
23. G. E. Thomas and K. Stamnes, *Radiative Transfer in the Atmosphere and Ocean* (Cambridge University, 1999).
24. C. D. Mobley, *Light and Water, Radiative Transfer in Natural Waters* (Academic, 1994).
25. A. D. Clarke, C. McNaughton, V. Kapustin, Y. Shinozuka, S. Howell, J. Dibb, J. Zhou, B. Anderson, V. Brekhovskikh, H. Turner, and M. Pinkerton, "Biomass burning and pollution aerosol over North America: organic components and their influence on spectral optical properties and humidification response," J. Geophys. Res. **112**, D12S18 (2007).
26. O. L. Hadley, C. E. Corrigan, and T. W. Kirchstetter, "Modified thermal-optical analysis using spectral absorption selectivity to distinguish black carbon from pyrolized organic carbon," Environ. Sci. Tech. **42**, 8459–8464 (2008).
27. T. C. Bond, "Spectral dependence of visible light absorption by carbonaceous particles emitted from coal combustion," Geophys. Res. Lett. **28**, 4075–4078 (2001).
28. R. W. Bergstrom, P. Pilewskie, P. B. Russell, J. Redemann, T. C. Bond, P. K. Quinn, and B. Sierau, "Spectral absorption properties of atmospheric aerosol," Atmos. Chem. Phys. **7**, 5937–5943 (2007).
29. P. B. Russell, R. W. Bergstrom, Y. Shinozuka, A. D. Clarke, P. F. DeCarlo, J. L. Jimenez, J. M. Livington, J. Redemann, O. Dubovik, and A. Strawa, "Absorption Angstrom exponent in AERONET and related data as an indicator of aerosol composition," Atmos. Chem. Phys. **10**, 1155–1169 (2010).
30. M. O. Andreae and A. Gelencsér, "Black carbon or brown carbon? The nature of light-absorbing carbonaceous aerosols," Atmos. Chem. Phys. **6**, 3131–3148 (2006).
31. H. Sun, L. Biedermann, and T. C. Bond, "Color of brown carbon: a model for ultraviolet and visible light absorption by organic carbon aerosol," Geophys. Res. Lett. **34**, L17813 (2007).
32. T. W. Kirchstetter, T. Novakov, and P. V. Hobbs, "Evidence that the spectral dependence of light absorption by aerosols is affected by organic carbon," J. Geophys. Res. **109**, D21208 (2004).
33. E. M. Patterson, D. A. Gillette, and B. H. Stockton, "Complex index of refraction between 300 and 700 nm for Saharan aerosols," J. Geophys. Res. **82**, 3153–3160 (1977).
34. T. C. Grenfell and D. K. Perovich, "Incident spectral irradiance in the Arctic Basin during the summer and fall," J. Geophys. Res. **113**, D12117 (2008).
35. P. Ricchiazzi, S. Yang, C. Gautier, and D. Sowle, "SBDART: a research and teaching software tool for plane-parallel radiative transfer in the Earth's atmosphere," Bull. Am. Meteorol. Soc. **79**, 2101–2114 (1998).
36. Y. Shinozuka, A. D. Clarke, P. F. DeCarlo, J. L. Jimenez, E. J. Dunlea, G. C. Roberts, J. M. Tomlinson, D. R. Collins, S. G. Howell, V. N. Kapustin, C. S. McNaughton, and J. Zhou, "Aerosol optical properties relevant to regional remote sensing of CCN activity and links to their organic mass fraction: airborne observations over Central Mexico and the US West Coast during MILAGRO/INTEX-B," Atmos. Chem. Phys. **9**, 6727–6742 (2009).
37. D. A. Hegg, S. G. Warren, T. C. Grenfell, S. J. Doherty, and A. D. Clarke, "Sources of light-absorbing aerosol in arctic snow and their seasonal variation," Atmos. Chem. Phys. **10**, 10923–10938 (2010).